Thrust Control via Rotor Skewing in Integrated Twin Bearingless Motor

Nathan PETERSEN*, WaiYan CHAN* and Anvar KHAMITOV*
* Motibera, Inc.
3330 Marsh Rd, Madison, WI 53718, United States
E-mail: nathan@motibera.com

Abstract
This paper presents a practical method for achieving full five-degree-of-freedom (5-DOF) levitation control using a twin bearingless motor architecture. Bearingless motors inherently produce both torque and radial magnetic suspension forces, but conventional designs lack axial force capability. To address this limitation, this work proposes to introduce rotor skewing to generate axial thrust via torque-current excitation. A twin motor configuration with equal and opposite rotor skew enables net torque production through common-mode current excitation, while differential torque currents produce net axial force. Theoretical modeling is presented to highlight the electromagnetic mechanisms responsible for skew-induced axial force, and the design space is analyzed to maximize current-to-thrust efficiency. Finite element simulations quantify the effects of rotor skew angle on torque, radial force, and axial thrust production. A control scheme is presented which decouples torque and axial force through coordinated current excitation across both motor halves. Simulation results confirm that substantial axial force can be generated with minimal degradation of torque and radial bearing performance. A candidate design achieves axial force exceeding 5× the rotor weight under full differential excitation, requiring less than 20% of rated current to achieve axial levitation. These findings demonstrate the feasibility of skew-based axial force generation in twin bearingless motors, offering a compact and efficient solution for applications with moderate axial load demands.

Keywords : bearingless motor, magnetic levitation, axial force control, rotor skewing, 5-DOF levitation

1. Introduction

Bearingless motors combine electromagnetic torque production with active magnetic suspension, offering an elegant and compact solution for eliminating mechanical contact in rotating machinery. Traditional bearingless motor designs integrate radial magnetic bearing functions using the same motor materials (stator windings, iron, magnets) to achieve single-plane radial stabilization, while relying on additional actuators for axial and tilting support. As such, these systems are not truly "bearingless" in the full sense, and often require integration with active magnetic bearings (AMBs) to achieve full five-degree-of-freedom (5-DOF) levitation, i.e., center of mass translation in x-, y-, and z-axes, and tilting in α- and β-axes (Chiba et al. 2005). Although several design concepts have been proposed to address this limitation, they often introduce significant complexity in control, manufacturing, or both (Chen, J. Zhu, and Severson 2020).

One promising solution is the use of twin conical bearingless motors, which can generate axial and tilting forces through geometry-based field coupling (Munteanu, Binder, and Dewenter 2012; Munteanu 2013). Due to the conical design, the surface forces acting on the rotor have an axial component which enables thrust control. However, conical geometries are difficult to manufacture using standard laminated steel stacks, as they require non-uniform lamination sizes or post-machining to achieve the desired shape, both of which increase cost. Furthermore, in conical designs, all current components can contribute to axial forces, creating cross-coupling in control and complicating system stability (Messager and Binder 2017). The direct-axis current i_d contributes predominately to thrust forces, but other current components cross-couple depending on the specific motor design and geometry. Due to these limitations, an alternative approach that preserves manufacturing and control simplicity while enabling axial force control is desirable.

This work proposes and explores a practical solution (see Fig. 1) to address the above limitations by leveraging *rotor skew* to generate axial forces in a twin bearingless motor configuration. Skew is often used to limit torque ripple via reducing undesirable spatial harmonics in conventional motors (Müller et al. 2025; J. G. Lee, K. W. Lee, and G. S. Park 2013), however, here it is used intentionally to create controllable axial thrust through differential torque-current excitation.

The proposed architecture leverages symmetric, oppositely skewed rotors in a twin-motor arrangement, enabling common-mode torque current in both motor halves to control net torque, and differential current to produce net axial force. A similar concept was proposed in (Wu et al. 2015) with a twin opposite-skew design, but it did not actively control radial forces due to using passive permanent magnet radial bearings, and it leveraged a coreless stator, which is not scalable to practical applications. This paper proposes using standard laminated iron core and active 5-DOF control. Further, this work optimizes the design using both 2D and 3D finite element analysis (FEA) simulations to maximize axial force output. The result is a practical, manufacturable solution for achieving full 5-DOF levitation with low cross-coupling and minimal added complexity, making it suitable for applications with moderate axial loading.

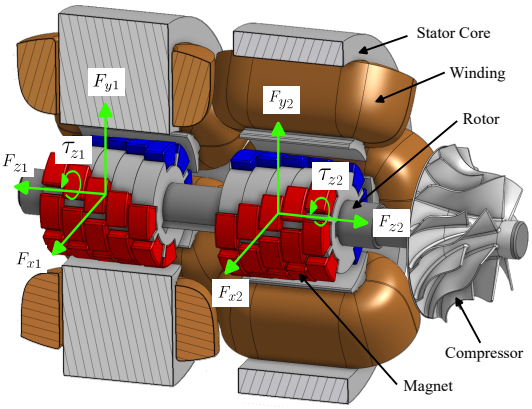

Fig. 1: Rendering of the proposed oppositely-skewed twin bearingless motor.

2. Theory of Operation

This section introduces the electromagnetic basis for axial force generation through rotor skewing in the proposed twin bearingless motor. While axial thrust in skewed machines has been previously reported in the literature (G.-J. Park, Kim, and Jung 2016; Kang et al. 2017), and similar ideas have been explored for bearingless motors (Wu et al. 2015), these works generally lack a detailed electromagnetic explanation or a clear formulation of the key influencing factors. This section aims to fill that gap by clarifying the physical mechanisms behind skew-induced axial force and identifying the parameters that govern its behavior, providing intuitive guidance for design and control.

2.1. Maxwell Stress Tensor and Field Interaction

Axial force is not typically produced in conventional non-skewed motors since their magnetic field distribution is largely confined to radial and tangential directions. While axial flux components appear near the stack ends due to fringing effects, axial symmetry ensures their net contribution averages to zero over the rotor length, resulting in negligible axial force. However, skewing the rotor magnets disrupts this axial symmetry. Mechanical skewing introduces a shift in the magnet edges along the axial direction by a skew angle γ, see Fig. 2a. This causes the magnetic flux density from the permanent magnets to develop an axial component B_z, in addition to the radial (B_r) and tangential (B_θ) components. The resulting axial force is created from the interaction between the radial and axial flux density components. This force is described by the Maxwell Stress Tensor, which in cylindrical coordinates includes a shear term that governs axial thrust:

$$\sigma_{zr}(\theta, z) = \frac{B_r(\theta, z) B_z(\theta, z)}{\mu_0}, \quad F_z = \iint_S \sigma_{zr}\, dS = \int_0^{2\pi} \int_{-L/2}^{L/2} \sigma_{zr}(\theta, z)\, r\, dz\, d\theta \tag{1}$$

where r is the airgap radius and μ_0 is the permeability of free space. The net axial force F_z is obtained by integrating the shear stress σ_{zr} over the cylindrical airgap surface, as shown in (1).

The B_z component is primarily localized near the stack ends (as in non-skewed machines) and at skewed magnet edges facing the airgap. As a result, the region of interest for evaluating axial force can be limited to these localized zones where the product $B_r B_z$ is non-zero. Accordingly, the total axial force can be approximated by calculating the contribution from a single skewed pole and scaling by the number of poles: $F_z = P F_{z,P}$. This provides a useful framework for studying axial force in skewed machines, which is illustrated further using finite element analysis (FEA) in the next subsection.

2.2. Thrust Mechanism Under Torque Excitation and Parameter Sensitivity

In the absence of stator excitation, axial flux components arise primarily at skewed magnet transitions and the stack ends. These form symmetric distributions of opposite sign, leading to local shear stresses that cancel out across the motor length. This behavior is demonstrated in the top row of Fig. 2b, using a 12-slot, 4-pole surface permanent magnet (SPM) motor as an example. The symmetric $B_r B_z$ distribution results in a negligible net axial force.

However, when a torque-producing i_q current is injected, the field distribution becomes asymmetric. The second row of Fig. 2b shows the resulting magnetic field and nodal force distributions. Notably, the forces at the skewed magnet edges remain relatively balanced and contribute minimally to net thrust. Instead, the dominant axial force arises from an imbalance between the upper and lower rotor ends. This imbalance is due to differences in the magnitude and spatial extent of B_z at the two ends, which are influenced by local B_r distribution and the effective magnetic reluctance of surrounding

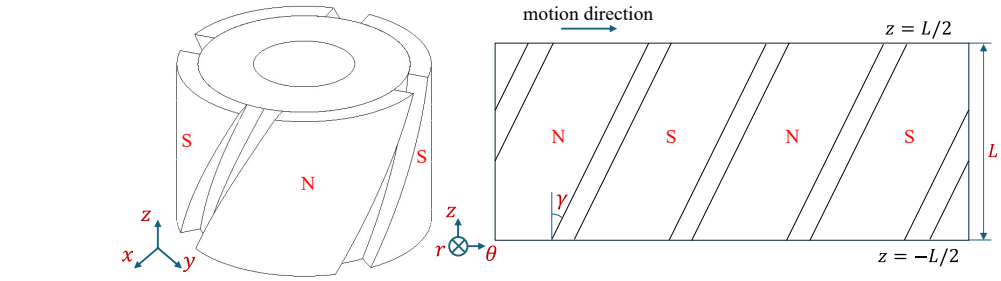

(a)

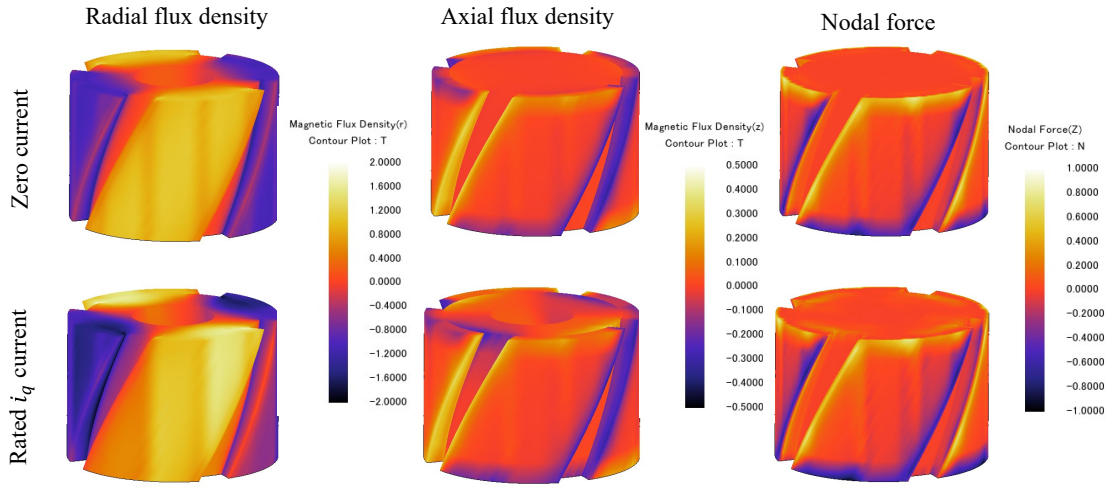

(b)

Fig. 2: Axial force creation in a skewed motor for an example 12-slot, 4-pole SPM motor: (a) illustration of a skewed rotor with 4 poles and definitions and (b) radial and axial magnetic flux density and resulting nodal force distribution in a skewed rotor with no stator current (row 1) and non-zero q-axis current (row 2).

paths, leading to unequal fringing behavior. The q-axis current exhibits spatial variation in radial flux density B_r along the axial direction. At the mid-plane ($z = 0$), the excitation corresponds closely to pure q-axis current, producing a moderate radial field. Toward the upper end region ($z = +L/2$), a portion of this excitation manifests as a d-axis component, effectively having a stronger radial field ($B_r^{(+)}$). Conversely, near the lower end region ($z = -L/2$), the radial field becomes weaker ($B_r^{(-)}$) due to the reverse effect. This variation in B_r influences the axial flux density B_z and modulates the resulting Maxwell shear.

To better understand the observed asymmetry in thrust, the axial force contribution from the unskewed stack-end slices is examined, where the axial flux arises predominantly due to fringing. In these regions, the axial flux density B_z may be approximated as proportional to the local radial flux density:

$$B_z^{(+)} = \kappa_+ B_r^{(+)}, \quad B_z^{(-)} = -\kappa_- B_r^{(-)} \tag{2}$$

Here, κ_+ and κ_- are dimensionless coefficients that capture local fringing behavior, permeability differences, and the extent of steel saturation. Asymmetries in κ can result from mechanical variations at the rotor ends—such as bulging into free air—or differing local operating points on the B-H curve, even when the skew angle corresponds to an integer slot pitch.

Using these definitions, the axial shear stresses near the bore at the two ends and the net axial force become:

$$\sigma_{zr}^{(+)} = \frac{\kappa_+ (B_r^{(+)})^2}{\mu_0}, \quad \sigma_{zr}^{(-)} = -\frac{\kappa_- (B_r^{(-)})^2}{\mu_0} \quad \Longrightarrow \quad F_z = \frac{1}{\mu_0}\left[\kappa_+ A_+ (B_r^{(+)})^2 - \kappa_- A_- (B_r^{(-)})^2\right]. \tag{3}$$

This combined expression captures the core trends seen in simulation. Although the upper end ($+z$) exhibits a stronger radial flux density $B_r^{(+)}$, it produces a smaller net force contribution due to a relatively low $\kappa_+ A_+$ product. In contrast, the lower end ($-z$), where $B_r^{(-)}$ is weaker, contributes more significantly to axial force due to a larger $\kappa_- A_-$ term. This outcome can be physically interpreted by considering that a weaker radial field implies less magnetic attraction between rotor and

stator at that end, allowing axial flux to fringe more freely. The result is a broader area of axial flux penetration and a correspondingly stronger axial force.

Since the radial flux at each end varies with torque-producing current i_q, the net axial force also varies accordingly. As i_q increases, the asymmetry in B_r between the two ends changes, modulating the individual terms in (3) and making axial thrust approximately proportional to torque. Among the key parameters influencing axial force density is the skew angle γ, which affects the development of axial flux near the end regions. Increasing γ initially enhances thrust by intensifying the asymmetry in field distribution, but the effect may saturate or reverse beyond a certain angle, depending on the magnet geometry and leakage paths. The ratio of rotor axial length to diameter (L/D) also plays a critical role. Since axial force is generated primarily at the end regions, shorter axial lengths improve the thrust-to-mass ratio. This favors compact designs for applications requiring active axial suspension or actuation.

Although this section introduces an intuitive formulation for axial thrust based on magnetic field interactions, accurate prediction still relies on detailed knowledge of local field distributions. These are best obtained using FEA. Section 4 presents a simulation-based study that optimizes the motor geometry and analyzes the axial force in a skewed rotor, focusing on the influence of skew angle and the rotor's aspect ratio.

3. Control Methodology

This section presents a simple control approach for achieving 5-DOF levitation and torque control using the proposed oppositely-skewed rotor twin topology. Torque and axial force are independently controlled through common- and differential-mode torque currents, with tradeoffs arising from shared current limits. Visualizations illustrate the coupling between torque and axial force production, as well as the implications for mechanical design and control implementation.

3.1. Operation of Motor System

The proposed motor system, illustrated in Fig. 1, consists of two identical but mirrored halves, with quantities denoted by subscripts "1" and "2" for segment 1 and 2. Each half functions as a complete, conventional single-plane bearingless motor, with field-oriented control implemented in its drive electronics. As is typical (Chiba et al. 2005), an inner current regulation loop exposes four current components (d, q, x, y) to an outer motion control loop. Torque τ_z is controlled with q-axis current: $\tau_{z1} = k_t i_{q1}$ and $\tau_{z2} = k_t i_{q2}$ with torque constant k_t in units of Nm/A. Field strength is controlled with d-axis current. Radial forces are controlled with x- and y-axis current: $F_{x1} = k_f i_{x1}$ and $F_{y1} = k_f i_{y1}$ with force constant k_f in units of N/A. Additionally, due to the rotor skew, the q-axis current also creates axial force F_z, but with opposite magnitude between the motor halves: $F_{z1} = k_z i_{q1}$ and $F_{z2} = -k_z i_{q2}$ with force constant k_z in units of N/A.

Since the control of radial force (F_x and F_y) is the same as typical bearingless motors and is decoupled from torque control, this work focuses only on the control of net axial force F_z and net torque τ_z. The net torque τ_z acting on the rotor is the sum of each motor half: $\tau_z = \tau_{z1} + \tau_{z2} = k_t(i_{q1} + i_{q2})$. The net axial force F_z on the rotor is also the sum of each motor half: $F_z = F_{z1} + F_{z2} = k_z(i_{q1} - i_{q2})$. It is clear that by carefully controlling each motor half's q-axis current, the net torque and force can be independently controlled. Inverting the above relations gives the key control equation which relates the desired net torque τ_z^* and net axial force F_z^* to the required current:

$$\begin{bmatrix} i_{q1}^* \\ i_{q2}^* \end{bmatrix} = \frac{1}{2} \begin{bmatrix} \frac{1}{k_t} & \frac{1}{k_z} \\ \frac{1}{k_t} & -\frac{1}{k_z} \end{bmatrix} \begin{bmatrix} \tau_z^* \\ F_z^* \end{bmatrix} \tag{4}$$

3.2. Tradeoffs Between Torque and Axial Force

Equation (4) indicates that the q-axis currents serve a dual role in the proposed motor architecture, simultaneously governing both torque and axial force. In the absence of axial force demands, the system behaves conventionally: each motor half contributes equally to the net torque. However, generating axial force *demands opposing torque* contributions from the two motor halves. In the limiting case, both halves operate at their current limits in opposition, yielding maximum axial force and zero net torque. Figure 3 shows the i_{q1}–i_{q2} control plane and the region allowed by the maximum current limit. Inside this region, contours of constant torque and axial force intersect, showing a tradeoff: increasing one reduces how much of the other is possible. The drive must split the available current between torque and axial force control, always staying within the current limit. The red and blue lines mark the highest achievable torque and axial force, highlighting that they cannot both be maximized at the same time. For example, operating at maximum axial force means no torque is available. This tradeoff is a key design constraint for systems that need both torque and axial force. Figure 4 shows the full control block diagram of the proposed solution, highlighting how both torque and thrust force commands determine the q-axis current commands.

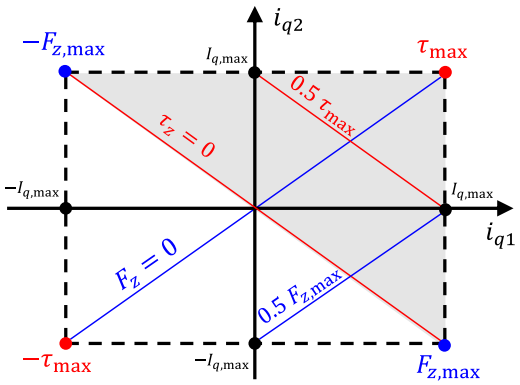

Fig. 3: Relationship between i_{q1} and i_{q2} and the resulting net torque and axial force operating regions.

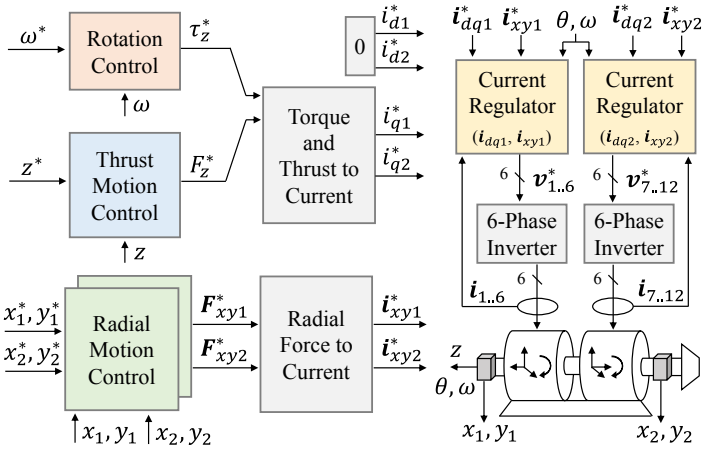

Fig. 4: Block diagram of full proposed 6-DOF control system.

Moreover, axial force generation introduces mechanically significant consequences: the two rotor halves must produce opposing torques, inducing torsional stress across the rotor shaft. The resulting internal torque differential is directly proportional to the axial force F_z and must be factored into the mechanical design. In the worst case, the shaft must be capable of withstanding the total differential torque, $\tau_{\max} = \tau_{z1} + \tau_{z2}$. Dynamic axial force output can cause stress fatigue in the shaft: if not properly handled during the design phase, this can reduce operating lifetime.

4. FEA Simulation Study

This section presents a two-stage optimization framework for a bearingless SPM motor that integrates torque production, radial suspension, and axial thrust. It begins by defining key design objectives and performance constraints, including torque-per-volume, force-to-rotor-weight ratio, and force vector error. A 2D FEA-based optimization is used to identify designs that maximize torque while meeting radial levitation requirements. The selected design is then extended to a 3D model with rotor skewing to evaluate axial thrust capabilities. Finally, the impact of rotor geometry on axial force efficiency is examined by varying the rotor length-to-diameter ratio.

4.1. Design Objectives

The design of the proposed twin bearingless motor system must balance three competing functions: (1) power conversion (torque production), (2) radial bearing support (radial force output), and (3) thrust force support (axial force output). Achieving a high-performance design requires well-established design priorities and metrics that inform motor sizing and control strategy from the outset. When power conversion is the sole specified design criterion (as in traditional motors with bearings), motor sizing can be effectively guided by standard laws that incorporate torque density, electromagnetic loading, and thermal limitations (Pyrhonen, Jokinen, and Hrabovcova 2013). However, adding radial force production (as in traditional bearingless motors) introduces *additional* constraints that require modifications to the motor design. There are two key metrics that must be optimized in bearingless motors: (1) maximizing the radial force density, i.e., the radial force-per-rotor-weight FRW_r at a fixed suspension current usage, and (2) minimizing the radial force ripple, i.e., radial force vector error magnitude and angle.

Typically, in horizontally mounted motors, radial forces in bearingless motors are used to overcome gravity to suspend the rotor. While other radial force loads exist, e.g., rotor imbalance and aerodynamic loads, this work normalizes the radial force output relative to the rotor weight, evaluated at a fixed ratio of suspension current. Geometric modifications to the rotor/stator which maximize radial force output are non-obvious, since it scales inversely with rotor radius (Chan, Noguchi, and Severson 2024). Prior studies (Chen, Fujii, et al. 2021; Chen, J. Zhu, and Severson 2020) have demonstrated that, with the implementation of combined (single) windings, only 2.5% to 5% of the total rated current is required to generate adequate radial suspension force, i.e., $\mathrm{FRW}_r \geq 1$. The remaining 95% of current is used for torque production. To preserve the desired torque output, an increase in rotor volume becomes necessary, and is typically achieved through a 5% extension of the motor's axial length.

Beyond meeting static performance requirements described above, dynamic stability, particularly with respect to force ripple, must also be rigorously addressed. Analogous to torque ripple, variations in suspension force arise from spatial harmonics in the air gap flux, resulting in periodic deviations of the force vector during each rotor revolution.

These deviations are quantified by the force vector error, typically characterized by two key metrics: the error magnitude E_m and the error angle E_a. The error magnitude E_m is directly analogous to torque ripple and represents the magnitude deviation from the average force vector over a rotation. The error angle E_a represents the maximum angular displacement between the actual and intended force vectors over a rotation, and is especially critical for maintaining robust suspension control. Excessive values of E_a, i.e., $E_a > 17°$, have been shown to induce instability in active magnetic suspension systems (Chiba et al. 2005). To ensure stable levitation and precise force control, bearingless motor designs typically aim to minimize E_a such that $E_a < 5°$ under nominal operating conditions (Jastrzebski et al. 2017).

While radial suspension in bearingless motors has been widely explored, enabling effective axial force support remains a key challenge in achieving fully bearingless operation. Conventional approaches rely on either additional thrust magnetic bearings, mechanical thrust bearings, or passive magnetic attraction. In contrast, the proposed design generates axial thrust within the motor using differential I_q current, eliminating the need for external components. This self-contained capability is characterized by the axial force constant $k_z = F_z/I_q$ where F_z is the generated axial force for an applied I_q current. A higher k_z reflects a more efficient conversion of current into axial thrust, enabling axial load support, but requires careful design trade-offs to balance torque and thrust performance. The axial thrust requirements vary drastically between applications since they are based on the system, e.g., aerodynamic loads in compressors. In this work, the axial force output is normalized by the rotor weight, i.e., FRW_z, to enable comparison to the radial force capability. Similar to the radial system, this work aims to maximize FRW_z at a given differential I_q current usage.

4.2. Optimization Study

To evaluate the performance potential of the proposed integrated bearingless motor, a two-stage optimization strategy is adopted. The first stage employs rapid 2D FEA simulations to identify a configuration that maximizes torque density while satisfying radial suspension requirements. This optimal design is then extended into a 3D model to assess axial thrust capability. Rotor skewing is introduced to induce axial force, and 3D FEA is used to quantify the resulting thrust. Although axial performance is not explicitly optimized, this approach reveals the inherent axial force characteristics of a design prioritized for radial performance. This two-stage framework enables decoupled evaluation of torque and thrust while maintaining computational efficiency.

This study investigates a 12-slot, 4-pole (Q12p2) SPM motor architecture featuring N42-grade NdFeB magnets and a $m = 6$-phase combined multi-phase stator winding capable of simultaneously generating both torque and radial suspension force. The key geometric design variables are shown in Fig. 5 and bounded in Table 1, with a fixed axial stack length of 100 mm applied across all candidates. Simulations assume a uniform stator current density of 10 $\mathrm{A_{rms}/mm^2}$, with 95% of the rated current allocated to torque and remaining 5% to radial suspension. Each design is evaluated under 2D FEA at a fixed rotor speed of 10 kr/min with no eddy currents enabled.

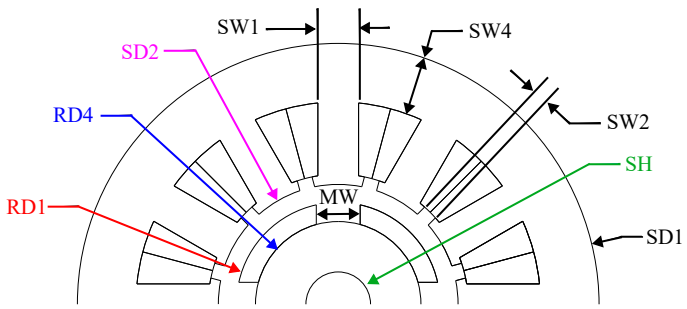

Fig. 5: SPM geometry with key design variables.

Table 1: Design variable bounds for $\boldsymbol{x}$. In mm.

Variable	Symbol	LB	UB
Stator OD	SD1	205	205
Stator ID	SD2	62	95
Tooth Width	SW1	5.5	8
Slot Opening Width	SW2	1	3
PM Gap	MW	3	13
Rotor PM OD	RD1	60	93
Rotor Core OD	RD4	55	89
Shaft Diameter	SH	25	32

The first optimization stage aims to maximize performance by increasing the torque-per-rotor-volume (TRV) ratio while minimizing total ohmic and core electromagnetic power losses $P_{\mathrm{loss}} = P_{\mathrm{Cu}} + P_{\mathrm{Fe,rotor}} + P_{\mathrm{Fe,stator}}$. This is formulated as a constrained multi-objective problem, as defined in (5). Constraints include limits on torque ripple, force vector error (E_a, E_m), and a minimum FRW_r to ensure radial levitation. Design variables $\boldsymbol{x}_j$ are bounded by their respective lower and upper limits, LB_j and UB_j.

$$\min_{\boldsymbol{x}} \begin{bmatrix} P_{\mathrm{loss}}(\boldsymbol{x}) \\ -\mathrm{TRV}(\boldsymbol{x}) \end{bmatrix} \text{ subject to: } \mathrm{LB}_j \le x_j \le \mathrm{UB}_j,\ T_{\mathrm{ripple}}(\boldsymbol{x}) \le 20\%,\ E_a(\boldsymbol{x}) \le 10°,\ E_m(\boldsymbol{x}) \le 20\%,\ \mathrm{FRW}_r(\boldsymbol{x}) \ge 1 \tag{5}$$

The optimization is carried out in JMAG using a multi-objective genetic algorithm (MOGA) with a population of 90 over 200 generations. Figure 6 illustrates the resulting design space, with feasible solutions in blue and the Pareto front in red. The selected design, marked with a star, achieves the highest TRV of 191 kNm/m^3. Its cross-sectional geometry is shown in Fig. 7, with dimensions and performance metrics listed in Tables 2 and 3.

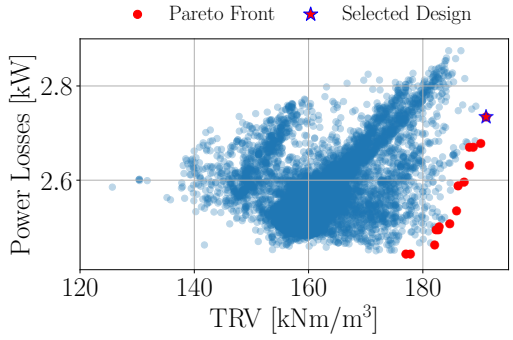

Fig. 6: Optimized design space.

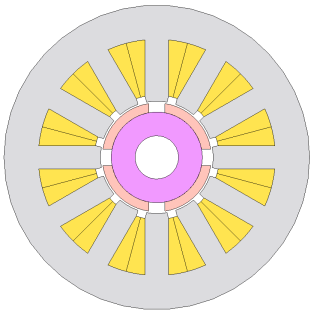

Fig. 7: 2D cross-section of the selected optimal design.

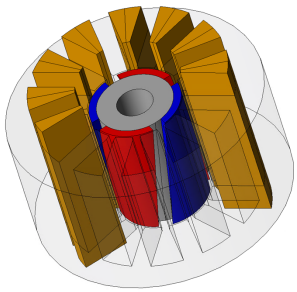

Fig. 8: 3D model of selected design with rotor skew.

Table 2: Dimension of optimized design. In units of mm.

Variable	SD1	SD2	SW1	SW2	MW	RD1	RD4	SH
Value	205	75.7	7.85	3	5.5	73.2	61.1	29.2

Table 3: Performance of optimized design.

Metric	T [Nm]	F_r [N]	TRV [kNm/m^3]	FRW [-]	P_{loss} [kW]	E_a [°]	E_m [%]
Value	80.6	103	191	3.17	2.74	9.4	17

The 2D-optimized design is extended to 3D (see Fig. 8) to evaluate axial force characteristics, introducing PM skewing to generate thrust and assess optimal skew angles. Figure 9 shows the impact of skew angle on key metrics, including torque, radial and axial forces, axial force-to-weight ratio FRW$_z$, and k_z. At a skew angle of 60° with 95% I_q current excitation, the design achieves an axial force F_z = 140 N with a corresponding FRW$_z$ = 4.3 and k_z = 12.7 N/A, demonstrating the effectiveness of skewing for axial suspension. However, this enhancement comes with moderate reductions in torque and radial force relative to the no-skew baseline. At 60° skew, average torque drops from 80 Nm to 65 Nm (-18.8%), and radial force from 100 N to 88 N (-12%). These reductions are primarily due to the attenuation of the fundamental air-gap flux component caused by PM skewing (Z. Q. Zhu and Howe 2007). The reductions reflect a trade-off intrinsic to skew-based axial force generation; however, they remain modest within the overall performance envelope and are considered acceptable given the substantial axial thrust achieved.

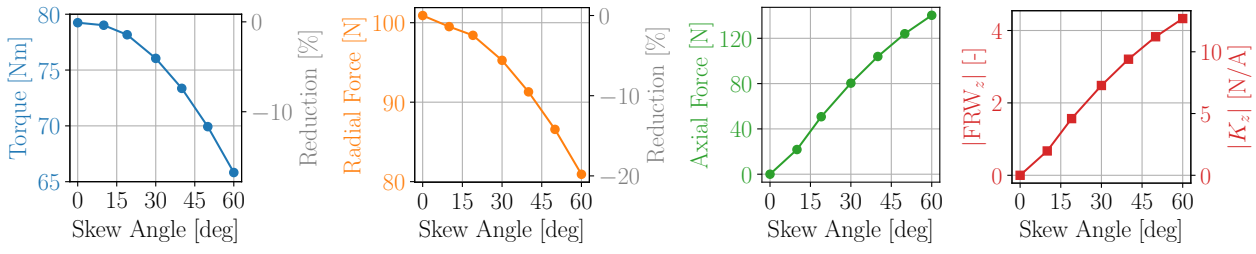

Fig. 9: Impact of rotor skew angle on motor performance. (a) Torque and (b) radial force decrease with skew, while (c) axial thrust increases due to asymmetry. (d) FRW$_z$ and axial force constant k_z improve.

While effective, the skew-based strategy raises questions about axial force density and current usage impacting overall motor efficiency. With FRW$_z$ = 4.3 at rated I_q current, approximately $\frac{1}{4.3}$ = 23.3% of the rated I_q current is required to counteract gravity, i.e., FRW$_z$ = 1. In contrast, radial suspension achieves FRW$_r$ ≥ 1 using only 5% of the current. From a force density perspective, this disparity highlights that axial force density is 4–5 times lower than radial. In an attempt to improve this disparity, the rotor length is varied and diameter is held constant to achieve a range of rotor length to diameter ratio L/D with 60° skew. Figure 10 shows this result when L/D ratio is varied from 0.5 to 2, and I_q current is its rated value. It can be observed that as L/D decreases towards flatter/shorter aspect ratio, the FRW$_z$ increases: at L/D = 0.5, the FRW$_z$ = 7.5, or equivalently, FRW$_z$ = 1 (counteract gravity) with only $\frac{1}{7.5}$ = 13.3% current.

This trend aligns with theoretical expectations: while radial forces scale with rotor surface area, axial thrust arises predominantly from interactions at the rotor ends. As a result, only the magnetized tips contribute meaningfully to axial force, limiting the effective active length. Shorter rotors, with a larger fraction of magnetized mass near the ends, concentrate force production and enhance FRW_z. In contrast, longer rotors dilute this effect, reducing axial force per unit weight. These findings underscore the critical role of rotor sizing in applications demanding high axial thrust.

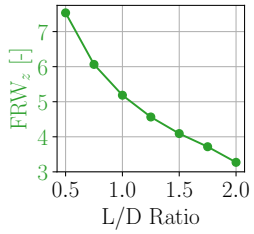

Fig. 10: Rotor L/D vs. FRW_z.

5. Conclusion

This work presents a practical method for achieving full five-degree-of-freedom levitation in bearingless motors by leveraging rotor skew in a twin-motor configuration. Differential q-axis currents across oppositely skewed rotors produce net axial thrust, while common-mode excitation yields net torque, enabling independent control of both quantities. Analytical modeling and 3D finite element analysis confirm that substantial axial force can be generated with modest current and minimal degradation in torque or radial force performance. A key finding is that axial forces originate from fringing flux at the rotor tips rather than the main air gap, so thrust does not scale with rotor volume—shorter rotors have more fringing effects, so achieve higher thrust-to-weight ratios. The optimized design achieves axial thrust exceeding 5x the rotor weight, and can support the rotor weight axially with less than 20% of rated current. The proposed architecture offers a manufacturable and low-complexity solution for integrated thrust control in compact, oil-free rotating systems.

Portions of this paper were drafted with the help of large language model (LLM) tools, including ChatGPT by OpenAI.

References

Chan, W., T. Noguchi, and E. L. Severson (2024). "Scaling of High-Speed Surface PM Bearingless Machines". In: *2024 IEEE Energy Conversion Congress and Exposition (ECCE)*, pp. 5631–5638.

Chen, J., Y. Fujii, et al. (2021). "Optimal Design of the Bearingless Induction Motor". In: *IEEE Transactions on Industry Applications* 57.2, pp. 1375–1388.

Chen, J., J. Zhu, and E. L. Severson (2020). "Review of Bearingless Motor Technology for Significant Power Applications". In: *IEEE Transactions on Industry Applications* 56.2, pp. 1377–1388.

Chiba, A. et al. (2005). *Magnetic bearings and bearingless drives*. Newnes.

Jastrzebski, R. P. et al. (2017). "Design of 6-slot inset PM bearingless motor for high-speed and higher than 100kW applications". In: *2017 IEEE International Electric Machines and Drives Conference (IEMDC)*, pp. 1–6.

Kang, C. H. et al. (2017). "Axial unbalanced magnetic force in a permanent magnet motor due to a skewed magnet and rotor eccentricities". In: *IEEE Transactions on Magnetics* 53.11, pp. 1–5.

Lee, J. G., K. W. Lee, and G. S. Park (2013). "Effects of V-Skew on the Torque Characteristic in Permanent Magnet Synchronous Motor". In: *Proceedings of the Int. Conf. on Electrical Machines and Systems*. Vol. 2. 4, pp. 390–393.

Messager, G. and A. Binder (2017). "Derivation of forces and force interferences in a double conical high-speed bearingless permanent magnet synchronous motor". In: *2017 IEEE Int. Elec. Machines and Drives Conf. (IEMDC)*.

Müller, K. et al. (2025). "Evaluation of Torque Ripple and Tooth Forces of a Skewed PMSM by 2D and 3D FE Simulations". In: *Scientific Computing in Electrical Engineering SCEE 2024*.

Munteanu, G. (2013). "Five-Axis Rotor Magnetic Suspension with Bearingless PM Motor Levitation Systems". PhD thesis. Institut für Elektrische Energiewandlung, TU Darmstadt.

Munteanu, G., A. Binder, and S. Dewenter (2012). "Five-axis magnetic suspension with two conical air gap bearingless PM synchronous half-motors". In: *International Symposium on Power Electronics Power Electronics, Electrical Drives, Automation and Motion*, pp. 1246–1251.

Park, G.-J., Y.-J. Kim, and S.-Y. Jung (2016). "Design of IPMSM applying V-shape skew considering axial force distribution and performance characteristics according to the rotating direction". In: *IEEE Transactions on Applied Superconductivity* 26.4, pp. 1–5.

Pyrhonen, J., T. Jokinen, and V. Hrabovcova (2013). *Design of rotating electrical machines*. John Wiley & Sons.

Wu, G. et al. (2015). "Design and analysis of a novel axial actively regulated slotless skew winding bearingless motor". In: *2015 IEEE International Conference on Mechatronics and Automation (ICMA)*, pp. 1864–1869.

Zhu, Z. Q. and D. Howe (2007). "Electrical Machines and Drives for Electric, Hybrid, and Fuel Cell Vehicles". In: *Proceedings of the IEEE* 95.4, pp. 746–765.